Ab initio parameterized valence force field for the structure and energetics of amorphous SiO_{x} (0 $\leqslant$ x $\leqslant$ 2) materials

Sangheon Lee, Robert J. Bondi, and Gyeong S. Hwang

Ab Initio Parameterized Valence Force Field for the Structure and Energetics of Amorphous SiO$_x$ (0 ≤ x ≤ 2) Materials

Sangheon Lee, Robert J. Bondi, and Gyeong S. Hwang*

Department of Chemical Engineering, University of Texas, Austin, Texas 78712, USA

We present a modified valence force field model for the structure and energetics of amorphous silicon suboxides (*a*-SiO$_x$, 0 ≤ x ≤ 2). The parameters are optimized to fit the results from cluster and periodic density functional theory (DFT) calculations of various model structures. The potential model well reproduces the DFT energetics of various *a*-SiO$_x$ systems for all O/Si composition ratios. We also examine how the choice of force fields affects the atomic-level description of phase separation in *a*-SiO$_x$ and *a*-Si/*a*-SiO$_2$ interfaces using a continuous random network model-based Monte Carlo approach. The results highlight the critical role of the relative rigidity between Si and SiO$_2$ matrices in determination of the structural properties of the Si/SiO$_2$ composite system, such as interface bond topology, degree of phase separation, and abruptness of the interface.

*Author to whom correspondence should be addressed:

e-mail: gshwang@che.utexas.edu

I. INTRODUCTION

Amorphous silicon-rich oxides (a-SiO$_x$, $0 \leq x \leq 2$) have garnered great attention not only from their unique properties, but also potential technological importance in various electronic, optoelectronic, and energy applications. Amorphous phases lack long range order or well-defined atomic structure and are thermodynamically less favorable than their corresponding crystalline phases.[1,2] As a consequence of lattice distortion and variations in composition, a-SiO$_x$ materials typically have different properties from their crystalline counterparts and also Si/SiO$_2$ multiphase systems. The properties of a-SiO$_x$ can be controlled by varying Si:O composition ratio and incorporating various impurities. For instance, hydrogenated a-SiO$_x$ materials exhibit visible room temperature photoluminescence (PL) properties and a higher photosensitivity than other materials with comparable optical gaps, making them viable candidates for Si-based optoelectronic applications.[3,4] In addition, doping with boron or phosphorous atoms might enable realization of light-emitting diodes.[5]

Si suboxides may undergo phase separation to yield oxide-embedded Si nanoparticles during high temperature annealing; the Si nanoparticles (np-Si) can be amorphous or crystalline depending on the annealing temperature.[6,7] The np-Si/a-SiO$_2$ system emits visible PL with high efficiency at room temperature, while luminescence from bulk crystalline Si (c-Si) is negligible as a result of its indirect band structure. The discovery of Si-based luminescence has generated considerable interest in its potential application to integrated optoelectronic devices.[8-10] In addition, oxide-embedded Si nanoparticles have been envisioned as possible discrete storage elements in non-volatile flash memories.[11,12] Earlier studies[13] have suggested that the performance of np-Si based devices would be determined by a complex combination of the following attributes: Si particle size, shape, and crystallinity; Si/SiO$_2$ interface structure and strain; and

near-interface defects (bonding, chemical, and structural). It is therefore important to develop a detailed understanding of the structure, strain, and composition of a-SiO$_x$ materials and their interfaces.

An atomic level understanding of a-SiO$_x$ materials derived from experimental methods has thus far remained elusive in part from the limited capabilities of common instrumentation for direct characterization. A complementary computational effort has been made in the development of atomistic models of amorphous materials in a variety of systems. First-principles methods have achieved widespread usage in characterization of the structure and properties of complex materials including multicomponent amorphous alloys.[14] Despite the enormous growth in computational power, highly disordered materials are often cost-prohibitive to address exclusively with first-principles calculations because realistic models of their structures typically contain complex topologies requiring large numbers of atoms. As an alternative to first-principles calculations, computationally less expensive classical force fields have been widely used; various types of interatomic potentials have been developed for Si,[15-21] SiO$_2$,[22-25] and Si/SiO2 composites.[26-29]

The primary liability in application of force fields is their limited transferability. Even for Si, no single force field model could provides an adequate description of the physical and chemical properties in all relevant states (from bulk, (crystal, amorphous, liquid), surfaces to clusters) of this prototypical semiconductor; consequently, it would be reasonable to conclude that generation of a single force field that comprehends all pertinent phenomena is likely an insurmountable task. Therefore, it would be necessary to develop application-specific potentials that, for instance, can be robustly-applied to describe the atomic structure and energetics in designated systems.

a-Si[1,2,30] and *a*-SiO$_2$[31,32] are well known to form respective Si and SiO$_4$ tetrahedral networks characterized by both long-range disorder and short-range order similar to that of their parent crystals. At Si/SiO$_2$ interfaces, previous experiments[33,34] have demonstrated extremely low densities (typically between 10^{10} to 10^{12} cm^{-2}) of interface defects, suggesting an almost-perfect bonding network across the interface. Likewise, *a*-SiO$_x$-based systems can also be well-represented by fully-coordinated random networks in which Si and O atoms are four and twofold coordinated, respectively. To generate a structural model of *a*-SiO$_x$, molecular dynamics (MD) or Monte Carlo (MC) methods coupled to various interatomic potentials have been widely used as detailed in the following work: (1) *ab-initio* MD for *a*-Si, [35] *a*-SiO$_2$,[36] and planar *c*-Si/*a*-SiO$_2$[37]; (2) classical MD for *a*-Si,[21] *a*-SiO$_2$,[25] planar *c*-Si/*a*-SiO$_2$,[27,29,38,39] and *np*-Si/*a*-SiO$_2$[40,41]; and (3) classical MC for *a*-Si,[16,42] *a*-SiO$_2$,[22] *a*-SiO$_x$,[43] planar *c*-Si/*a*-SiO$_2$,[26,44,45] and *np*-Si/*a*-SiO$_2$.[45-47] *Ab-initio* MD permits accurate description of atomic arrangements, but its utility is restricted to small systems and short time scales because of steep computational requirements. Classical MD permits simulation of relatively large systems, but the same time scale limitations could compromise complete structural relaxation. Classical MC based on a continuous random network (CRN) model is a proven approach for the construction of fully-relaxed *a*-SiO$_x$ structures.[26,42,46,48,49] Within the CRN model, an amorphous system is relaxed via a large number of bond transpositions using Metropolis Monte Carlo (MMC) sampling,[42] where the validity of the final structure also strongly depends on application of a reliable force field. Since this approach does not require description of bond formation/scission, simple and computationally less expensive valence force field (VFF) models like the three-body, harmonic Keating-like (KT) potentials have been widely used, permitting simulation of larger systems. Effective VFF models are currently available for prediction of minimum-energy configurations of fully-coordinated Si- and

SiO$_2$-based materials when the bond lengths and angles do not significantly deviate from their equilibrium values[16,22]; however, relatively little effort has been undertaken to assess and improve the accuracy of existing VFF models for a-SiO$_x$-based systems.

In this paper, we present a valence force field based on a modified Keating model for the structure and energetics of amorphous Si rich oxide (a-SiO$_x$, $0 \leq x \leq 2$) materials. We optimize the parameters to fit the results from cluster and periodic density functional theory (DFT) calculations of various model structures. In order to evaluate the reliability of our potential, we prepare model structures for a-SiO$_x$ ($x = 0, 0.5, 1, 1.5,$ and 2) using CRN-MMC simulations based on the present potential and compare their energetics with the energetics from DFT and earlier Keating-like and modified Stillinger-Weber potential calculations. We also examine how the choice of force fields affects the atomic-level description of phase separation in a-SiO$_2$ and a-Si/a-SiO$_2$ interfaces. We prepare model structures for oxide-embedded amorphous Si nanoparticles using CRN-MMC simulations based on the present potential and earlier Keating-like potential models and subsequently characterize the structural models in terms of concentration of suboxide states (Si^{1+}, Si^{2+}, Si^{3+}), strain energy profiles, and ring-size distributions. To explain the observed structural properties, we use relative rigidities of bulk a-Si and bulk a-SiO$_2$ which are obtained by calculating their mechanical properties. Based on these results, we assess the role of strain in determination of the structural properties of the Si/SiO$_2$ composite system, such as interface bond topology, degree of phase separation, abruptness of the interface.

II. CALCULATION METHODS

A. Valence force field model for a-SiO$_x$ ($0 \leq x \leq 2$)

Within the VFF model, the relative energies of a-SiO$_x$ materials are evaluated in terms of the increase of total energy (ΔE_{total}) with respect to the Si-Si and Si-O bond energies obtained respectively from c-Si and c-SiO$_2$ (β-cristobalite in this work). The ΔE_{total} can be given by the sum of the changes in strain energy (ΔE_{strain}) and suboxide energy (ΔE_{subox}):

$$\Delta E_{total} = \Delta E_{strain} + \Delta E_{subox}. \tag{1}$$

The suboxide (penalty) energy (ΔE_{subox}) represents an increase in the Si-Si and Si-O bond energies arising from the various oxidation states of Si.[50] For a given Si-rich suboxide system, ΔE_{subox} can be obtained by adding the suboxide penalties of individual Si atoms with intermediate oxidation states (+1, +2, +3). Using periodic c-SiO$_x$ (x = 0.5, 1.0, and 1.5) models (see FIG. 2 in 48), our DFT calculations predict the suboxide energies of 0.54, 0.57, and 0.29 eV for Si^{1+}, Si^{2+}, and Si^{3+}, respectively, in good agreement with previous DFT results.[50-52]

Strain energy (ΔE_{strain}) arises from lattice distortions involving bond stretching, bond angle distortion, torsion resistance, and non-bonding interactions. The structure, stability, and phonon properties of bulk disordered Si and SiO$_2$ materials have been successfully studied using a Keating-like VFF model:

$$E_{strain} = \frac{1}{2}\sum_i k_b (b_i - b_0)^2 + \frac{1}{2}\sum_{i,j} k_\theta (\cos\theta_{ij} - \cos\theta_0)^2 , \tag{2}$$

where k_b (in eV/Å^2) and k_θ (in eV) refer to the bond-stretching and angle-distortion force constants, respectively, b_i and b_0 (in Å) are the lengths of the ith bond and the equilibrium (reference) bond, respectively, and θ_{ij} and θ_0 (in degrees) are the angles subtended by the ith and j^{th} bonds and the equilibrium bond angle, respectively. The three-body harmonic potential offers a satisfactory description of the strain of Si and SiO$_2$ materials particularly when the departure of the bond lengths and bond angles from their respective equilibrium values is insignificant.[16,22]

For strain and suboxide energy variations, Keating-like (KT) potentials have been applied to examine the network topology and properties of a-Si and a-SiO$_2$.[26,44,46] In particular, the KT potential parameterized by Tu and Tersoff [referred to as KT(TT), hereafter] has been widely employed to determine the atomic structure and energetics of amorphous Si/SiO$_2$ multiphase systems, including planar c-Si/a-SiO$_2$ interfaces[26,53] and np-Si/a-SiO$_2$.[46] For the present work, first Lee and Hwang optimized KT potential parameters based on the geometries and energies from density-functional theory (DFT) calculations [referred to as KT(LH) to distinguish it from KT(TT)]. This optimization procedure is detailed in the following section.

Earlier studies emphasized the importance of k_θ for the Si-O-Si bond angle to achieve a realistic description of bulk a-SiO$_2$. The relatively small k_θ(Si-O-Si) value in the KT(TT) potential appears to result in a large discrepancy between experimental and simulation results for the Si-O-Si bond angle distribution in the highly-distorted a-SiO$_2$ network, which was corrected by making the k_θ(Si-O-Si) term stronger [22] Compared to bulk a-SiO$_2$, we expect the SiO$_2$ structure near the Si/SiO$_2$ interface to be more distorted due to strain arising from the lattice mismatch between Si and SiO$_2$. Therefore, an improved description of Si-O-Si bond angle distortion is likely warranted to obtain more realistic structural models and energetics for Si/SiO$_2$ interface systems. Likewise, other angle distortion force constants (such as k_θ(O-Si-O), k_θ(Si-Si-O), and k_θ(Si-Si-Si)) might also require reexamination since bond topologies and strain energies in a-SiO$_x$ materials are mainly governed by three-body contributions. In addition, the equilibrium Si-Si and Si-O bond lengths are known to be a function of Si charge state.[34,50,51] It is reasonable to infer that optimization of b_0(Si-Si) and b_0(Si-O) values in terms of Si oxidation state might be influential; however, we will later show that equilibrium bond length variations are insignificant as well as their influence on the suboxide structure.

B. Determination of force field parameters

The potential parameters are determined by fitting VFF total energy data to DFT values in the following sequence that corresponds to an increase in the degrees of freedom of each training set: (1) b_0(Si-Si) and b_0(Si-O); (2) k_b(Si-Si) and k_b(Si-O); (3) θ_0(Si-Si-Si); θ_0(O-Si-O), θ_0(Si-O-Si), and θ_0(Si-Si-O); (4) k_θ(Si-Si-Si); (5) k_θ(Si-O-Si) [and also n_θ(Si-O-Si), power of the three-body term]; (6) k_θ(O-Si-O); and (7) k_θ(Si-Si-O). Table I summarizes the force constant values for both the KT(LH) and KT(TT) potentials along with other KT potential parameters for bulk a-SiO$_2$. Table II likewise summarizes calculated and tabulated b_0 values.

For determination of b_0(Si^m-Si^n) and b_0(Si^m-O), where m and n indicate the oxidation states of respective Si atoms, we used periodic crystalline Si^0, Si^{1+}, Si^{2+}, Si^{3+}, and Si^{4+} lattice models (see Fig. 2 in Ref. 52) as well as cluster models for all oxidation states (see Figure 1). When $m = n$, the b_0 values can be obtained from periodic calculations. Assuming that the variation of b_0 with Si oxidation state is identical for the periodic and cluster calculations, we tabulated the b_0 values when $m \neq n$ based on the cluster calculation results:

$$b_0(m,n) = \frac{b_0(n,n)\{B_0(m,m) - b_0(m,n)\} + b_0(m,m)\{B_0(m,n) - B_0(n,n)\}}{B_0(m,m) - B_0(n,n)}, \qquad (3)$$

where b_0 and B_0 refer to the equilibrium bond lengths from our periodic and cluster calculation results, respectively. The b_0(Si^m-O) value decreases with increasing m, possibly attributed to a reduction in the contribution of covalency, consistent with previous *ab initio* calculations.[34,50,51] We observe the contribution of oxidation state to insignificantly affect the resultant a-SiO$_x$ bond topology as corroborated by minor perturbations (substantially less than 0.1 Å) in average Si^m-Si^n and Si^m-O bond lengths.

For $k_b(Si^0-Si^0)$ and $k_b(Si^{4+}-O)$ parameters, we calculated variations in the total energies of

c-Si (with 8 atoms) and c-SiO$_2$ (β-cristobalite with 8 SiO$_2$ units) by varying their respective lattice constants from -5% to 5%. For DFT calculations, a Monkhorst-Pack (8×8×8) k-point mesh was used for Brillouin-zone sampling. Optimized values of $k_b(Si^0-Si^0)$ = 9.08 eV/Å^2 and $k_b(Si^{4+}-O)$ = 31.90 eV/Å^2 are close to corresponding KT(TT) values as shown in Table I. For c-Si and c-SiO$_2$, the variation of ΔE computed by KT(LH), KT(TT), and DFT calculations is shown in Figs. 2(a) and 2(b), respectively, as a function of the magnitude of bond strain. For both model systems, the VFF values are in good agreement with DFT values near equilibrium. The potential dependence of k_b on Si oxidation state was also examined using cluster model calculations. From our results, k_b appears inversely proportional to b_0; however, the magnitude of k_b variation is sufficiently small, so we can safely disregard the oxidation effect.

With the equilibrium bond angle of θ_0(Si-Si-Si) = 109.5°, we optimized the force constant k_θ(Si-Si-Si) using four independent 64-atom a-Si supercells. The optimal value was obtained through minimization of the cross-validation error (ξ) which is given by:

$$\xi^2 = \frac{1}{N} \sum_{n=1}^{N} (E_{DFT}^{(n)} - E_{FF}^{(n)})^2 , \tag{4}$$

where $E_{DFT}^{(n)}$ and $E_{FF}^{(n)}$ refer to the DFT and FF energies, respectively, of the nth of N total a-Si models in the training set; in this case, the energies were evaluated based on fully-relaxed structures (with the same network) from each calculation. The same procedure was applied in optimization of other k_θ values, unless stated otherwise. Our optimized k_θ(Si-Si-Si) value of 1.795 eV is only half of the corresponding KT(TT) value of 3.58 eV. This is not surprising considering that a-Si is softer than c-Si, while the KT(TT) value well reproduces the crystalline Si properties.

For the remaining three-body force constants, equilibrium bond angles were set at θ_0(O-Si-O) = 109.5°, θ_0(Si-Si-O) = 109.5°, and θ_0(Si-O-Si) = 180°, which are well-established for the

Si-O system. Given that both Si-O-Si and O-Si-O bond angle distortions contribute to the ener-getics of a-SiO$_2$, we first determined k_θ(Si-O-Si) using a cluster model structure [see Figure 3 inset], then computed k_θ(O-Si-O) using four independent, periodic a-SiO$_2$ model structures (each containing 64-SiO$_2$ units).

From our DFT cluster calculations [see Figure 3], the total energy only slightly changes as θ(Si-O-Si) is reduced from 180° to 150°, but rapidly increases for θ(Si-O-Si) < 120°. The KT(TT) values of k_θ(Si-O-Si) = 0.75 eV and n_θ(Si-O-Si) = 2 (power of the corresponding three-body term) show reasonable agreement with DFT results for $150^\circ < \theta$(Si-O-Si) $\leq 180^\circ$, yet exhi-bit significant underestimation for θ(Si-O-Si) < 150°. Many previous studies[54-56] have demon-strated that the amorphous silica structure has a wide Si-O-Si angle distribution that may vary from 120° to 180°. Note that θ(Si-O-Si) can be around 130° and 160°, respectively, in three- and four-membered rings in a-SiO$_2$. To more rigorously describe the strain energy variation asso-ciated with the wide distribution of the O-subtended bond angle, we adjusted not only k_θ(Si-O-Si), but also n_θ(Si-O-Si), in the three-body term, $k_\theta(\cos\theta - \cos\theta_0)^{n_\theta}$. By fitting VFF total ener-gies to DFT values from the cluster and subsequent periodic calculations, we obtained k_θ(Si-O-Si) = 2.62 eV and n_θ(Si-O-Si) = 2.2. Note that these parameters are comparable to k_θ(Si-O-Si) = 2.0 eV with n_θ(Si-O-Si) = 2 from a careful reoptimization for a-SiO$_2$ bulk phases by Alfthan et $al.$[22] Concomitantly, we obtained k_θ(O-Si-O) = 10.25 eV, which is also much larger than 4.32 eV from KT(TT), using four independent periodic a-SiO$_2$ model structures. We also adjusted k_θ(Si-O-Si) and k_θ(O-Si-O) simultaneously using four independent, periodic a-SiO$_2$ model struc-tures, but found that the optimized values were essentially unchanged. Finally, we determined k_θ(Si-Si-O) = 4.165 eV using four independent, periodic a-SiO models comprised of 64 Si-O units, which is close to the KT(TT) value of 3.93 eV.

C. Metropolis Monte Carlo simulations

All a-SiO$_x$ structures we present were generated by CRN-MMC simulations (in the isothermal and isochoric ensemble) combined with either KT(LH) or KT(TT) potentials. The atomic structure of each model system evolves toward thermodynamic equilibrium though MC bond-switching moves,[42] which we implemented using the extended WWW (Wooten-Winer-Weaire) bond transposition scheme.[16] A bond switching move involves two bonds, A-B and C-D, across four unique atoms (A, B, C, and D) and forms two new bonds B-D and A-C by severing bonds A-B and C-D. A sampling process selects one of five different combinations of four distinct atoms (A, B, C, and D): Si(A)-Si(B)-Si(C)-Si(D); O(A)-Si(B)-O-Si(C)-O(D); Si(A)-Si(B)-Si(C)-O(D); Si(A)-Si(B)-O(C)-Si(D); and O(A)-Si(B)-Si(C)-O(D), where atoms A and C, as well as atoms B and D, must not be directly connected by a bond prior to the switching maneuver. For O(A)-Si(B)-O-Si(C)-O(D), the O atom between atom B and atom C is first selected randomly, then the remaining atoms are randomly identified. For the remaining combinations, either atom B or C is first selected randomly, then the remaining atoms are randomly identified. The acceptance or rejection of each bond-switching move is determined using probability $P = min[1, exp(-\Delta E/k_B T)]$, where ΔE is the change in ΔE_{total} resulting from the bond-switching move. Before and after each bond-switching move, the system is relaxed by Polak and Ribiere's conjugate-gradient method.[57]

During the MMC simulation, we included an additional repulsive term (E_r) in ΔE_{total} to effectively prevent nonbonded atoms from interacting.[16,26] Inclusion of E_r is particularly important in a-SiO$_x$ topological determination, likely because the flexible Si-O-Si linkages permit much more structural degrees of freedom than fourfold-coordinated a-Si. The repulsive contribution is given by:

$$E_r = \gamma \sum_{mn} (d_2 - r_{mn})^3 , \qquad (6)$$

where m and n denote atoms which are neither 1st nor 2nd neighbors in the network, r_{mn} is the distance between two atoms (evaluated only for $r_{mn} < d_2$), and d_2 is a cutoff distance. We used the following parameters: d_2(Si-Si) = 3.84 Å, d_2(Si-O) = 3.2 Å, d_2(O-O) = 2.61 Å, and $\gamma = 0.5$ eV/Å^3, referring to Ref. 16 and 22. The E_r term becomes negligible for the well-relaxed a-SiO$_x$ models presented in this paper.

The following procedure was used for construction of each a-SiO$_x$ ($0 \leq x \leq 2$) structure model. First, we began with a randomized Si configuration in a periodic supercell with volume (V) given by $V = V_{Si} \times N_{Si}$, where N_{Si} denotes the number of Si atoms and V_{Si} is the unit volume of a-Si. The randomized Si configuration was sequentially relaxed at temperatures of 5000, 4000, 3000, 2000, and 1000 K with approximately 1000$\times N_{Si}$ trials for each temperature. Next, N_O (= xN_{Si}) O atoms were randomly incorporated into Si-Si bonds in the a-Si model, resulting in an intermediate a-SiO$_x$ model with volume (V) given by $V = V_{Si} \times (N_{Si} - N_O/2) + V_{SiO2} \times N_O/2$, where V_{SiO2} denotes the unit volume of a-SiO$_2$. V_{Si} and V_{SiO2} were extracted from corresponding experimental densities of 2.28 g/cm^3 and 2.2 g/cm^3, respectively.[30,58] This intermediate configuration was further relaxed in a thermal sequence of 5000, 4000, 3000, 2000 and 1000 K with approximately 200($N_{Si} + N_O$) trials for each temperature. Each time the simulation temperature was decremented, the lowest-energy configuration from the completed temperature step was selected as the initial configuration for the ensuing simulation step. The MC simulations were conducted in a canonical ensemble (NVT); after the initial (highly distorted or nearly random) structures were relaxed, we also conducted the simulations allowing volume relaxation in all three directions, but the key structural properties from the isobaric simulations were nearly indistinguishable from the isochoric cases.

D. Density-functional theory calculations

All DFT calculations herein were performed using the well-established planewave pro-gram, VASP,[59] within the generalized gradient approximation of Perdew and Wang (GGA-PW91).[60] Vanderbilt-type ultrasoft pseudopotentials[61] were adopted to describe the interaction between ion cores and valence electrons. Valence electron wave-functions were expanded using a planewave basis set with a kinetic-energy cut-off of 400 eV. For Brillouin zone sampling, we used a (2×2×2) Monkhorst-Pack k-point mesh for all periodic a-SiO$_x$ supercell models with 64 Si and 64x O atoms (sufficient for disordered systems) and Γ-point sampling for cluster models, unless noted otherwise. All structures were fully-relaxed using the conjugate gradient method until residual forces on constituent atoms became smaller than 5×10^{-2} eV/Å.

III. RESULTS AND DISCUSSION

A. Energetics of amorphous SiO$_x$: Comparisons between force field models and DFT

We evaluated the reliability of the force fields considered in this work for the energetics of a-SiO$_x$ materials by comparison with DFT results. Besides KT(LH) and KT(TT), we also looked at extended Stillinger-Weber (SW) potentials without and with considering the suboxide penalty as proposed by Watanabe $et\ al.$[27,28]; for convenience, the former and latter are referred to as WT1 and WT2, hereafter.

First, we prepared model structures for a-SiO$_x$ (x = 0, 0.5, 1, 1.5, and 2) using MC simu-lations based on the KT(LH) potential without including ΔE_{subox} to avoid suboxide phase separa-tion into Si and SiO$_2$. For x = 0.5, 1, and 1.5, the prevailing Si oxidation states are +1, +2, and +3, respectively, as listed in Table III; in the model structures, O atoms are almost evenly distri-buted. For each x, we considered four independent structures each of which contains 64 Si atoms with 64x O atoms.

Figure 4 shows the variations of $\Delta \hat{E}_{total}$ (= ΔE_{total} per Si atom) with x from DFT, KT(LH), KT(TT), WT1, and WT2 calculations. The DFT result (distribution) in Fig. 4 resembles a parabola with maximum at $x \approx 1$, driven mainly by suboxide penalty contribution (later demonstrated in Fig. 5). Among the four classical potentials, KT(LH) exhibits the best agreement with DFT for all a-SiO$_x$ models. KT(TT) tends to overestimate and underestimate the total energies of a-Si and a-SiO$_2$, respectively. As expected, WT1 (with no suboxide penalty contribution) yields no significant variation in $\Delta \hat{E}_{total}$ with x, while WT2 (whose pair-like interaction term was modified in order to describe the suboxide penalty[28,62]) significantly overestimates the suboxide contribution. In addition, compared to DFT, both WT1 and WT2 are likely to underestimate $\Delta \hat{E}_{total}$ in a-Si, while showing relatively good agreement in a-SiO$_2$.

Figure 5(a) presents the average strain energies per Si ($\Delta \hat{E}_{strain}$) from KT(LH), KT(TT), and DFT calculations, which were obtained by subtracting the average suboxide penalty energies (in the inset) from the average total energies (in Fig. 4). For each x, average values represent four independent structures considered. Overall, KT(LH) and DFT are in good agreement. Compared to KT(LH) and DFT, KT(TT) yields a noticeably larger $\Delta \hat{E}_{strain}$ value in a-Si, where $\Delta \hat{E}_{strain}$ monotonically decreases with increasing O content and becomes smallest in a-SiO$_2$. The ΔE_{strain} overestimation of KT(TT) for a-Si is mainly attributed to the larger k_θ(Si-Si-Si) value of 3.58 eV relative to 1.795 eV in KT(LH), while the underestimated ΔE_{strain} in a-SiO$_2$ is due to the smaller k_θ(Si-O-Si) and k_θ(O-Si-O) values of 0.75 eV and 4.32 eV relative to the respective values of 2.62 eV (with n_θ = 2.2) and 10.25 eV in KT(LH). Note that the two-body force constants, k_b(Si-Si) and k_b(Si-O), are comparable for KT(TT) and KT(LH).

We repeated the above procedure using model structures with partial phase separation which were obtained from MC simulations including ΔE_{subox} in KT(LH). For each x, four inde-

pendent structures were considered. As summarized in Table IV, the Si oxidation state statistics clearly indicate the formation of Si and SiO_2 phases in the suboxide systems. Figure 5(b) shows the variations of $\Delta\hat{E}_{strain}$ (and $\Delta\hat{E}_{subox}$ in the inset) as a function of Si:O ratio (x) from KT(LH), KT(TT), and DFT calculations. For the suboxide systems, KT(LH) shows excellent agreement with DFT, but the KT(TT) values significantly deviate from the DFT and KT(LH) values.

It is worth noting that ΔE_{strain} increases while ΔE_{subox} drops in the phase separation of suboxides, as seen from the separation-induced changes of $\Delta\hat{E}_{strain}$ and $\Delta\hat{E}_{subox}$ [Figure 5(a) vs. Figure 5(b)]. For instance, the phase separation results in an increase in $\Delta\hat{E}_{strain}$ from 0.127 to 0.225 eV/Si when $x = 1$ (i.e., a-SiO), while $\Delta\hat{E}_{subox}$ reduces by 0.227 eV/Si. These results suggest that the role of strain might be important in determining the atomic configurations, particularly in the Si/SiO_2 interface region, although the phase separation is mainly driven by the reduction of suboxide penalty energy.[52]

B. Phase separation: a-Si cluster embedded in a-SiO_2 matrix

In this section, we examine how the atomic-level description of phase separation in a-SiO_2 is affected by the choice of force fields. In particular, based on the KT(LH) and KT(TT) potentials, we attempt to assess the role of strain in determination of the atomic configuration near the Si/SiO_2 interface. For both KT(LH) and KT(TT) potentials, we constructed five independent phase-separated model structures using CRN-MMC simulations. The structure generation procedure adopted the following steps for each model: (i) construction of a 480-atom a-Si supercell; (ii) insertion of 720 O atoms into Si-Si bonds from the supercell perimeter inward with concurrent volume compensation (following $V = V_{Si}\times(N_{Si} - N_O/2) + V_{SiO2}\times N_O/2$ from Sec. II C); (iii) execution of O atom hopping moves at 100 K over $200(N_{Si} + N_O)$ trials to induce further

15

phase separation (only ΔE_{subox} was considered, not ΔE_{strain}, to expedite phase separation); (iv) implementation of bond-switching moves within the oxide phase through a thermal sequence of 5000, 4000, 3000, 2000, and 1000K over approximately 200(N_{Si} + N_O) trials for each temperature; and (v) completion of bond-switching maneuvers throughout the supercell (both phases) in consecutive thermal stages of 3000, 2000, and 1000K over approximately 200(N_{Si} + N_O) trials for each temperature. Each time the simulation temperature changed, the lowest-energy configuration from the prior simulation was adopted as the initial configuration for the subsequent simulation stage. This extensive approach provides a thorough description of phase separation in the a-SiO$_{1.5}$ suboxide that leads to the formation of an a-Si cluster embedded in a a-SiO$_2$ matrix. Example configurations from our simulations are presented in Fig. 6.

Comparing the phase-separated structures from KT(LH) and KT(TT) potential-based simulations (referred to as KT(LH) and KT(TT) models, hereafter), we find important discrepancies in the degree of phase separation (identifiable by the distribution of intermediate Si oxidation states) as well as the distribution of ring sizes. In Table V, we summarize the relative concentrations of Si oxidation states for the KT(LH) and KT(TT) models. While Si^{3+} is the dominant suboxide state in both models because of its low suboxide energy (0.29 eV) relative to those of Si^{1+} (0.54 eV) and Si^{2+} (0.57 eV), the overall concentration of suboxide states (Si^{1+}, Si^{2+}, Si^{3+}) is higher in the KT(LH) model than the KT(TT) model. In addition, Table V shows that each suboxide state is more abundant in the KT(LH) model relative to the KT(TT) model. To provide some quantification of the abruptness of the phase transition interface regions, we calculated ratios of Si/SiO$_2$ states (Si^0, Si^{4+}) to suboxide states (Si^{1+}, Si^{2+}, Si^{3+}) as 0.78 and 0.81 for the KT(LH) and KT(TT) models, respectively. These results suggest that the KT(LH) model should

16

yield more graded Si/SiO$_2$ interface profiles with smaller a-Si cluster phases than KT(TT) models.

To further characterize the suboxide transition interface, we provide energy and Si suboxide distribution profiles in Figs. 7 and 8, respectively, along radial directions from the a-Si cluster centers for both models. As shown in Fig. 7, the a-SiO$_2$ region in the KT(TT) model exhibits much higher $\Delta\hat{E}_{strain}$ values, but less Si suboxide penalty contributions, than the KT(LH) model; however, the KT(TT) model a-Si region exhibits lower $\Delta\hat{E}_{strain}$ values than observed in the KT(LH) model. We also observe that both a-Si and a-SiO$_2$ regions in the proximity of the Si/SiO$_2$ interfaces yield higher strain energies than bulk a-Si and a-SiO$_2$.

In Fig. 8, the radial profiles of Si suboxide distribution clarify the inferences about phase transition abruptness extracted from the suboxide distribution results compiled in Table V. For each model, we define a nominal interface radius, r_0, that effectively defines a reference for the Si/SiO$_2$ interface,

$$r_0 = \frac{\sum r(Si^{1+}) + \sum r(Si^{2+})}{n(Si^{1+}) + n(Si^{2+})}, \tag{7}$$

where $r(Si^m)$ is the distance of a Si atom with oxidation state m from the cluster center, $n(Si^m)$ is the number of Si^m, and the summations are conducted over all four independent samples studied. The Si^{1+} and Si^{2+} states can be interpreted as perimeter Si atoms of the a-Si phase with one and two O neighbors, respectively. For the Si^{3+} oxidation state, the increased spread in radial distribution of the KT(LH) model over the KT(TT) model is readily apparent in Fig. 8. For both models, we observe a prominent peak in the Si^{3+} oxidation state just outside of r_0. The KT(LH) Si^{3+} distribution also exhibits a more graded phase transition interface since the KT(LH) model has both a lower peak and a more significant distribution tail on the a-SiO$_2$ side ($r - r_0 > 5$Å) when contrasted to the KT(TT) distribution.

17

In Fig. 9, we present ring-size distributions for the (a) total, (b) a-Si, and (c) a-SiO$_2$ components of the KT(LH) and KT(TT) model structures. For the a-Si and a-SiO$_2$ cases, the paths comprised solely of Si^0 and Si^{4+} atoms are counted as rings, respectively; for comparison, the ring-size distributions of bulk a-Si and a-SiO$_2$ are also provided. For a-Si, the embedded phase contains more five-membered rings in both models, rather than the energetically-favored six-membered rings that are most frequently observed in bulk a-Si. Likewise, the a-SiO$_2$ phase in the two-phase system yields broader ring size distributions than in bulk a-SiO$_2$ for both models. This indicates that the phase-separated Si and SiO$_2$ structures are more strained than their bulk counterparts. We also notice in the a-Si phase that the KT(LH) model structures tend to contain more five-membered rings than the KT(TT) model structures; on the other hand, the latter generally exhibit broader ring size distributions than the former in the a-SiO$_2$ phase. This is not surprising considering that the KT(LH) potential over- and underestimates lattice strain in a-SiO$_2$ and a-Si, respectively, compared to the KT(TT) potential.

C. Mechanical Properties

Our calculations suggest that the relative rigidity between Si and SiO$_2$ matrices is critical in determination of the Si/SiO$_2$ interface structure. Elastic (or Young's) modulus (Y) and bulk modulus (B) are important metrics of the rigidity of an elastic response. For various a-SiO$_x$ compositions, these two moduli were successfully evaluated by first-principles calculations using a statistical approach in our previous work[63] and the endpoint cases ($x = 0$ and 2) have been well-characterized through experimental measurements.[64-69] Additional mechanical properties, such as the Poisson ratio (v) and shear modulus (G), can be calculated once Y and B are known because only two of these four quantities are independent in isotropic materials.[63] We apply our

previously reported moduli calculation method to VFF total energy data to evaluate Y and B

based on both KT(LH) and KT(TT) potentials for a-Si and a-SiO$_2$ in order to quantify the degree

of rigidity in respective a-Si and a-SiO$_2$ matrices.

The elastic (or Young's) modulus (Y) was calculated by computing forces and stresses

from VFF total energy (E) data using the following relationships:

$$F_x = \frac{\partial E_x}{\partial x}\bigg|_{x=\varepsilon} \tag{8}$$

$$\sigma_{xx} = \frac{F_x}{A} \tag{9}$$

$$Y = \frac{\sigma_{xx}}{\varepsilon} \tag{10}$$

Forces along a given direction (F_x) were calculated for each strain condition (ε) using second or-

der numerical derivatives in Eq. (8), normal stresses (σ_{xx}) were subsequently evaluated with Eq.

(9) (A represents the supercell face area in the x direction), and ultimately Young's modulus is

obtained from Eq. (10) as the ratio of stress to strain in the x direction. To provide adequate sta-

tistical sampling of Y for each structure sample, Y was evaluated at each condition for -5% $\leq \varepsilon \leq$

5% at 0.5% intervals, and an average Y is obtained.

The bulk modulus (B), which is the 3-D analog of Y, can be calculated from total energy

data as

$$B = V \frac{\partial^2 E}{\partial V^2}\bigg|_{V=V_i} = \frac{\partial E / \partial V}{\Delta V / V_o} = \frac{\text{volumetric stress}}{\text{volumetric strain}} , \tag{11}$$

where V_o is the equilibrium cell volume, $\varepsilon_v = \Delta V/V_o$ is an arbitrary volumetric strain, and V_i is the cell volume at an arbitrary ε_v. Similar to our treatment of Y, B was evaluated at each condition for $-5\% \leq \varepsilon_v \leq 5\%$ at 0.5% intervals, and an average B is obtained.

Table VI provides a summary of our mechanical property calculations along with relevant experimental data for comparison. The KT(LH) and KT(TT) potential-based calculations exhibit significant differences in Y and B values for both a-Si and a-SiO$_2$, where the former provides better agreement with experimental data than the latter. The similar B values for a-Si from KT(LH) and KT(TT) calculations can be attributed to nearly identical k_b values for the two potentials, suggesting that the bulk modulus is nearly unaffected by bond angle (Si-Si-Si) distortions. The remaining disparities for Y and B values in both a-Si and a-SiO$_2$ between KT(LH) and KT(TT) potentials can be clearly explained by the aforementioned differences in k_b and k_θ.

Considering the disparate nature of a-Si and a-SiO$_2$ in the local proximity of a Si/SiO$_2$ interface, the relative rigidity of SiO$_2$ to Si should be an important factor in structural determination of these interfaces. Since both bond (Si-Si and Si-O) stretching and angle (Si-Si-Si, O-Si-O, and Si-O-Si) distortion contribute to Young's modulus for a-Si and a-SiO$_2$, we attempted to quantify the relative rigidity between a-Si and a-SiO$_2$ using Y, rather than B. We evaluate the following dimensionless number, γ, as a measure of relative rigidity:

$$\gamma = \frac{Y_{a-SiO2}}{Y_{a-Si}}, \tag{12}$$

where $Y_{a\text{-Si}}$ and $Y_{a\text{-SiO2}}$ are the Young's moduli for bulk a-Si and bulk a-SiO$_2$, respectively. Our calculations show that a-Si (Y = 158.4 GPa) from KT(TT) is slightly more rigid than a-Si (Y = 124.3 GPa) from KT(LH), while a-SiO$_2$ (Y = 46.3 GPa) from KT(TT) is far less rigid than a-SiO$_2$ (Y = 98.9 GPa) from KT(LH). From these Y values, we obtain $\gamma_{KT(LH)} = 0.8$ and $\gamma_{KT(TT)} =$

0.3 for the KT(LH) and KT(TT) potentials, respectively. This indicates that the relative rigidity of SiO_2 to Si is significantly underestimated by KT(TT). The smaller $\gamma_{KT(TT)}$ implies that application of the KT(TT) potential will likely lead to structural rearrangement in the a-SiO_2 phase driven by minimization of strain exerted on the a-Si phase, ultimately resulting in excess distortion in the a-SiO_2 structure. In contrast, the larger $\gamma_{KT(LH)}$ implies that a similar driving force for a-SiO_2 structural distortion is significantly reduced for the KT(LH) potential. This provides a plausible explanation for the contrasting strain energy profiles of the KT(LH) and KT(TT) potentials as depicted in Fig. 7(a).

The occurrence of relatively more graded (abrupt) Si/SiO_2 interfaces for the KT(LH) (KT(TT)) model structures can be explained by the difference in rigidity between a-Si and a-SiO_2 phases. Phase separation of a-SiO_x into Si and SiO_2 phases is driven by minimization of the suboxide energy, but it concurrently creates additional distortion from lattice mismatch between Si and SiO_2; as a result, the increase of strain energy from lattice mismatch tends to temper the formation of abrupt boundaries. In application of the KT(TT) potential, the excessively pliable a-SiO_2 phase permits disproportionate lattice distortion on the a-SiO_2 side of the interface which leads the system to form relatively abrupt Si/SiO_2 interfaces. In contrast, in application of the KT(LH) potential, the relatively more rigid a-SiO_2 side of the interface is more resistive to accommodation of lattice distortion, so formation of relatively graded Si/SiO_2 interfaces is favored (see Fig. 8).

The CRN-MMC approach with a simple VFF model can provide a reasonable description of the defect free, minimum energy configurations of various Si/SiO_2 composite systems, which will further allow thorough studies of their optical and electrical properties and also the nature and behavior of defects and impurities in the complex system. However, the Si/SiO_2 interface

structure would also be influenced by process conditions; for instance, a significant amount of compressibility can be found in the SiO_2 region near the interface during oxidation of Si nanowires, when the rate of oxidation is greater than the rate of structural relaxation.[70] In those cases, not only thermodynamic equilibrium but also kinetics might need to be considered. Moreover, the Si/SiO_2 interface often contains a non-negligible amount of coordination defects due largely to lattice-mismatch-induced strains. To take into account the kinetic effect, it would be necessary to use more advanced methods such as molecular dynamics with a more sophisticated potential model.[29,71-73]

IV. SUMMARY

We present a valence force field based on a modified Keating model for the structure and energetics of amorphous Si rich oxide (a-SiO_x, $0 \leq x \leq 2$) materials. The potential parameters for the strain energy contribution were optimized to fit DFT results for various cluster and periodic model structures. Suboxide energies were determined using DFT calculations of periodic c-SiO_x ($x = 0.5$, 1.0, and 1.5) models, which are 0.54, 0.57, and 0.29 eV for Si^{1+}, Si^{2+}, and Si^{3+}, respectively. We particularly focused on precise optimization of bond angle force constants such as $k_\theta(\text{Si-O-Si})$, $k_\theta(\text{O-Si-O})$, $k_\theta(\text{Si-Si-O})$, $k_\theta(\text{Si-Si-Si})$ since bond topologies and strain energies in a-SiO_x are mainly governed by the three-body contributions. In this work, to more rigorously describe the strain energy variation associated with a wide Si-O-Si angle distribution (particularly in a highly strained Si/SiO_2 composite system), we adjusted not only $k_\theta(\text{Si-O-Si})$ but also $n_\theta(\text{Si-O-Si})$ in the three-body term, $k_\theta(\cos\theta - \cos\theta_0)^{n_\theta}$. We also considered variations in the equilibrium bond lengths such as $b_0(\text{Si-Si})$ and $b_0(\text{Si-O})$ in terms of Si oxidation state, but the contribution of oxidation state turns out to insignificantly affect the resultant a-SiO_x bond topology. For

the energetics of various a-SiO$_x$ ($0 \leq x \leq 2$) systems, the present potential model agrees well with DFT for all O/Si composition ratios, while earlier Keating-like and modified Stillinger-Weber potential models exhibit significant deviations from the present model and DFT. These results emphasize the importance of correctly describing the wide Si-O-Si angle distribution by making the corresponding bond-bending term stronger as well as softening of the Si lattice in the amorphous phase by making Si-Si-Si bond-bending term weaker. We also find that phase separation in a-SiO$_x$ results in an increase in the strain energy while the suboxide penalty decreases. Although the phase separation is mainly driven by the reduction of suboxide energy, our calculations demonstrate that the role of strain is important in determining the atomic configurations particularly in the highly strained Si/SiO$_2$ interface region. Our study also suggests that the relative rigidity between Si and SiO$_2$ matrices is critical in determination of the Si/SiO$_2$ interface structure. As such, as a measure of relative rigidity we introduced and evaluated a dimensionless number $\gamma = Y_{a-SiO2} / Y_{a-Si}$, where Y$_{a\text{-Si}}$ and Y$_{a\text{-SiO2}}$ are the Young's moduli for bulk a-Si and bulk a-SiO$_2$, respectively. From the present potential model, the value of γ is estimated to be 0.8 in the a-Si/a-SiO$_2$ system, and decreases in the c-Si/a-SiO$_2$ case. A smaller γ implies larger structural rearrangement in the SiO$_2$ part driven by minimization of strain exerted on the Si part, ultimately resulting in more distortion in the a-SiO$_2$ structure with a broader ring size distribution as well as a less graded Si/SiO$_2$ interface layer with a lower concentration of suboxide states (Si^{1+}, Si^{2+}, Si^{3+}). The present potential model coupled with the CRN-MMC method can be used to create structural models (free of coordination defects) for complex a-SiO$_x$-based materials, which will further allow thorough studies of the optical and electrical properties of these materials and also the nature and behavior of defects and impurities in the a-SiO$_x$ system. The VFF model could further be improved by taking into account additional penalty energy terms associated with poss-

ible coordination defects (such as divalent/trivalent Si and monovalent O defects) to address their effects on the structural properties and energetics. Moreover, by reoptimizing the force parameters the simple valence bond model can be applied to study the mechanical, thermal and vibrational properties of various a-SiO$_x$ systems.

While the CRN-MMC approach with a simple VFF model is designed to determine thermodynamically-equilibrated configurations, the structure of Si/SiO$_2$ composites can be often a function of process condition, for instance, during Si oxidation and SiO$_2$ deposition on Si; in those cases, not only thermodynamic equilibrium but also kinetics might need to be considered. To take into account the kinetic effect, it would be necessary to use more advanced methods such as molecular dynamics with a more sophisticated potential model.

REFERENCES

1. J. Fortner and J.S. Lannin, *Phys. Rev. B* **39**, 5527 (1989).

2. S. Kugler, G. Molnar, G. Petö, E. Zsoldos, L. Rosta, A. Menelle, and R. Bellissent, *Phys. Rev. B* **40**, 8030 (1989).

3. K.S. Min, K.V. Shcheglov, C.M. Yang, H.A. Atwater, M.L. Brongersma, and A. Polman, *Appl. Phys. Lett.* **69**, 2033 (1996).

4. E. Neufeld, S. Wang, R. Actz, Ch. Buchal, R. Carius, C.W. White, and D.K. Thomas, *Thin Solid Films* **294**, 238 (1997).

5. A.I. Belov, V.A. Belyakov, V.A. Burdov, A.N. Mikhailov, and D.I. Tetelbaum, *Journal of Surface Investigation-X-ray Synchrotron and Neutron Techniques* **3**, 627 (2009).

6. F. Iacona, C. Bongiorno, C. Spinella, S. Boninelli, and F. Priolo, *J. Appl. Phys.* **95**, 3723 (2004).

7. Y.Q. Wang, R. Smirani, and G.G. Ross, *J. Cryst. Growth* **294**, 486 (2006).

8. W.L. Wilson, P.F. Szajowski, and L.E. Brus, *Science* **262**, 1242 (1993).

9. Y. Kanemitsu, T. Ogawa, K. Shiraishi, and K. Takeda, *Phys. Rev. B* **48**, 4883 (1993).

10. L. Pavesi, L. Dal Negro, C. Mazzoleni, G. Franzo, and F. Priolo, *Nature (London)* **408**, 440 (2000).

11. M. Carrada, A. Wellner, V. Paillard, C. Bonafos, H. Coffin, and A. Claverie, Appl. Phys. Lett. 87, 251911 (2005).

12. S. Tiwari, F. Rana, H.I. Hanafi, A. Hartstein, E.F. Crabbe, and K. Chan, *Appl. Phys. Lett.* **68**, 1377 (1996).

13. L.C. Kimerling, L. Dal Negro, S. Saini, Y. Yi, D. Ahn, S. Akiyama, D. Cannon, J. Liu, J.G. Sandland, D. Sparacin, J. Michel, K. Wada, and M.R. Watts, *Silicon Photonics* (Springer-Verlag, Berlin, 2004).

14. M.C. Payne, M.P. Teter, D.C. Allan, T.A. Arias, and J.D. Joannopoulous, *Rev. Mod. Phys.* **64**, 1045 (1992).

15. P.N. Keating, *Phys. Rev.* **145**, 637 (1966).

16. Y. Tu, J. Tersoff, G. Grinstein, and D. Vanderbilt, *Phys. Rev. Lett.* **81**, 4899 (1998).

17. F.H. Stillinger and T.A. Weber, *Phys. Rev. B* **31**, 5262 (1985).

18. J. Tersoff, *Phys. Rev. B* **37**, 6991 (1988).

19. D.W. Brenner, *Phys. Rev. Lett.* **63**, 1022 (1989).

20. R. Biswas and D.R. Hamann, *Phys. Rev B* **36** (1987) 6434.

21. J.F. Justo, M.Z. Bazant, E. Kaxiras, V.V. Bulatov, and S. Yip, *Phys. Rev. B* **58**, 2539 (1998).

22. S. von Alfthan, A. Kuronen, and K. Kaski, *Phys. Rev. B* **68**, 073203 (2003).

23. S. Tsuneyuki, M. Tsukada, and H. Aoki, Y. Matsui, *Phys. Rev. Lett.* **61**, 869 (1988).

24. B.W.H. van Beest, G.J. Kramer, and R.A. van Santen, *Phys. Rev. Lett.* **64**, 1955 (1990).

25. K. Vollmayr, W. Kob, and K. Binder, *Phys. Rev. B* **54**, 15808 (1996).

26. Y. Tu and J. Tersoff, *Phys. Rev. Lett.* **84**, 4393 (2000).

27. T. Watanabe, H. Fujiwara, H. Noguchi, T. Hoshino, and I. Ohdomari, *Jpn. J. Appl. Phys., Part 2* **38**, L366 (1999).

28. T. Watanabe, D. Yamasaki, K. Tatsumura, and I. Ohdomari, *Appl. Surf. Sci.* **234**, 207 (2004).

29. A.C.T. van Duin, A. Strachan, S. Stewman, Q. Zhang, X. Xu, and W.A. Goddard, *J. Phys. Chem. A* **107**, 3803 (2003).

30. K. Laaziri, S. Kycia, S. Roorda, M. Chicoine, J.L. Robertson, J. Wang, and S.C. Moss, *Phys. Rev. B* **60**, 13520 (1999).

31. W.H. Zachariasen, *J. Am. Chem. Soc.* **54**, 3841 (1932).

32. B.E. Warren, H. Krutter, and O. Morningstar, *J. Am. Ceram. Soc.* **19**, 202 (1936).

33. E.H. Poindexter, P.J. Caplan, B.E. Deal, and R. Razouk, *J. Appl. Phys.* **52**, 879 (1981).

34. H. Fukuda, M. Yasuda, T. Iwabuchi, S. Kaneko, T. Ueno, I. Ohdomari, *J. Appl. Phys.* **72**, 1906 (1992).

35. I. Štich, R. Car, and M. Parrinello, *Phys. Rev. B* **44**, 11092 (1991).

36. J. Sarnthein, A. Pasquarello, and R. Car, *Phys. Rev. B* **52**, 12690 (1995).

37. A. Pasquarello, M.S. Hybertsen, and R. Car, *Nature (London)* 396, **58** (1998).

38. K. Tatsumura, T. Watanabe, D. Yamasaki, T. Shimura, M. Umeno, and I. Ohdomari, *Jpn. J. Appl. Phys., Part 1* **42**, 7250 (2003).

39. D. Fischer, A. Curioni, S. Billeter, and W. Andreoni, *Appl. Phys. Lett.* **88**, 012101 (2006).

40. J. Dalla Torre, J.-L. Bocquet, Y. Limoge, J.-P. Crocombette, E. Adam, G. Martin, T. Baron, P. Rivallin, and P. Mur, *J. Appl. Phys.* **92**, 1084 (2002).

41. M. Ippolito, S. Meloni, and L. Colombo, *Appl. Phys. Lett.* **93**, 153109 (2008).

42. F. Wooten, K. Winer, and D. Weaire, *Phys. Rev. Lett.* **54**, 1392 (1985).

43. V.M. Burlakov, G.A.D. Briggs, A.P. Sutton, and Y. Tsukahara, *Phys. Rev. Lett.* **86**, 3052 (2001).

44. K.O. Ng and D. Vanderbilt, *Phys. Rev. B* **59**, 10132 (1999).

45. L. Kong and L.J. Lewis, *Phys. Rev. B* **77**, 085204 (2008).

46. G. Hadjisavvas and P.C. Kelires, *Phys. Rev. Lett.* **93**, 226104 (2004).

47. F. Djurabekova and K. Nordlund, *Phys. Rev. B* **77**, 115325 (2008).

48. N. Mousseau and G.T. Barkema, *J. Phys. Cond. Matt.* **16**, S5183 (2004).

49. G.T. Barkema and N. Mousseau, *Phys. Rev. B* **62**, 4985 (2000).

50. D.R. Hamann, *Phys. Rev. B* **61**, 9899 (2000).

51. A. Bongiorno and A. Pasquarello, *Phys. Rev. B* **62**, R16326 (2000).

52. D. Yu, S. Lee, and G.S. Hwang, *J. Appl. Phys.* **102**, 084309 (2007).

53. Y. Tu and J. Tersoff, *Phys. Rev. Lett.* **89**, 086102 (2002).

54. J.R.G. DaSilva, D.G. Pinatti, C.E. Anderson, and M.L. Rudee, *Phil. Mag.* **31**, 713 (1975).

55. F. Mauri, A. Pasquarello, B.G. Pfrommer, Y.-G. Yoon, and S.G. Louie, *Phys. Rev. B* **62**, R4786 (2000).

56. R. Mozzi and B. Warren, *J. Appl. Crystallogr.* **2**, 164 (1969).

57. E. Polak, *Computational Methods in Optimization*, Academic Press, 1971.

58. J. Sarnthein, A. Pasquarello, and R. Car, *Phys. Rev. Lett.* **74**, 4682 (1995).

59. G. Kresse and J. Furthmuller, *VASP the Guide* (Vienna University of Technology, Vienna, 2001).

60. J.P. Perdew and Y. Wang, Phys. Rev. B 45, 13244 (1992).

61. D. Vanderbilt, *Phys. Rev. B* **41**, 7892 (1990).

62. J. Samela, K. Nordlund, V.N. Popok, E.E.B. Campbell, *Phys. Rev. B* **77**, 075309 (2008).

63. R.J. Bondi, S. Lee, and G.S. Hwang, *Phys. Rev. B* **81**, 195207 (2010).

64. M. Szabadi and P. Hess, *Phys. Rev. B* **58**, 8941 (1998).

65. D.M. Follstaedt, J.A. Knapp, and S.M. Myers, J. Mater. Res. 19, 338 (2004).

66. T. Rouxel, *J. Am. Ceram. Soc.* **90**, 3019 (2007).

67. H. Ni, X. Li, and H. Gao, *Appl. Phys. Lett.* **88**, 043108 (2006).

68. B. Bhushan, *Handbook of Nanotechnology* (Springer, Berlin, 2004), p. 773.

69. X. Li, B. Bhushan, K. Takashima, C.-W. Baek, and Y.-K. Kim, *Ultramicroscopy* **97**, 481 (2003).

70. H.I. Liu, D.K. Biegelsen, F.A. Ponce, N.M. Johnson, and R.F.W. Pease, *Appl. Phys. Lett.* **64**, 1383 (1994).

71. D.E. Yilmaz, C. Bulutay, and T. Cagin, *Phys. Rev.* B 77, 155306 (2008).

72. H. Ohta, T. Watanabe, and I. Ohdomari, *Jpn. J. Appl. Phys.* **46**, 3277 (2007).

73. S.R. Billeter, A. Curioni, D. Fischer, and W. Andreoni, *Phys. Rev. B.* **73**, 155329 (2006).

Table I. Optimized Keating-like potential force constants for the present work (referred to as KT(LH)) together with the optimized parameters of Ref. 26 (KT(TT)). The k_b are expressed in eV/Å^2 and the k_θ are in eV.

	KT(LH)	KT(TT)
k_b(Si-Si)	9.08	9.08
k_b(Si-O)	31.39	27.00
k_θ(Si-Si-Si)	1.80	3.58
k_θ(O-Si-O)	10.25	4.32
k_θ(Si-Si-O)	4.17	3.93
k_θ(Si-O-Si)	2.62[a]	0.75

a. The power of the three-body term is 2.2 (see the text).

Table II.   Calculated Si-Si and Si-O equilibrium bond distances from bulk structures with corresponding cluster values given in (). When $m \neq n$, $b_0(Si^m\text{-}Si^n)$ values for bulk structures are calculated based on the cluster calculation results using Eq. (3) (see the text). The b_0 are given in Å and the θ_0 are in degrees.

	b_0		θ_0	
$Si^0\text{-}Si^0$	2.362	(2.355)	Si-Si-Si	109.5
$Si^0\text{-}Si^{1+}$	2.373	(2.365)	O-Si-O	109.5
$Si^0\text{-}Si^{2+}$	2.375	(2.368)	Si-Si-O	109.5
$Si^0\text{-}Si^{3+}$	2.345	(2.346)	Si-O-Si	180.0
$Si^{1+}\text{-}Si^{1+}$	2.384	(2.379)		
$Si^{1+}\text{-}Si^{2+}$	2.385	(2.381)		
$Si^{1+}\text{-}Si^{3+}$	2.358	(2.359)		
$Si^{2+}\text{-}Si^{2+}$	2.385	(2.382)		
$Si^{2+}\text{-}Si^{3+}$	2.359	(2.360)		
$Si^{3+}\text{-}Si^{3+}$	2.335	(2.341)		
$Si^{1+}\text{-}O$	1.645	(1.642)		
$Si^{2+}\text{-}O$	1.632	(1.632)		
$Si^{3+}\text{-}O$	1.613	(1.619)		
$Si^{4+}\text{-}O$	1.593	(1.597)		

Table III. Si suboxide statistics for a-SiO$_{0.5}$ (64 Si and 32 O atoms), a-SiO$_{1.0}$ (64 Si and 64 O atoms), and a-SiO$_{1.5}$ (64 Si and 96 O atoms) structures used in Figs. 4 and 5(a). These structures were constructed from CRN-MMC simulations based on the KT(LH) potential excluding suboxide penalty energies. All values provided represent sampling over four independent structures in percentages (mean ± standard deviation).

	a-SiO$_{0.5}$	a-SiO$_1$	a-SiO$_{1.5}$
Si^0	26.6±4.0	3.1±1.1	0.4±0.7
Si^{1+}	49.2±6.1	26.6±2.9	1.6±1.6
Si^{2+}	22.2±2.0	42.2±4.3	21.8±4.3
Si^{3+}	1.6±1.1	23.4±6.2	50.0±6.6
Si^{4+}	0.4±0.7	4.7±2.9	26.2±3.0

Table IV. Si suboxide statistics for a-SiO$_{0.5}$ (64 Si and 32 O atoms), a-SiO$_{1.0}$ (64 Si and 64 O atoms), and a-SiO$_{1.5}$ (64 Si and 96 O atoms) structures used in Fig. 5(b). These structures were constructed from CRN-MMC simulations based on the KT(LH) potential including suboxide penalty energies.   All values provided represent sampling over four independent structures in percentages (mean ± standard deviation).

	a-SiO$_{0.5}$	a-SiO$_1$	a-SiO$_{1.5}$
Si^0	57.8±1.6	31.6±1.7	10.2±2.6
Si^{1+}	12.1±2.8	6.6±2.3	2.3±1.7
Si^{2+}	8.6±2.3	10.9±1.1	8.2±4.2
Si^{3+}	15.2±2.3	31.6±2.3	35.9±8.2
Si^{4+}	6.3±1.1	19.1±1.3	43.4±5.2

Table V. Si suboxide statistics sampled over five independent KT(LH) and KT(TT) models of np-Si/a-SiO$_2$ (480 Si and 720 O atoms) with quantities expressed as percentages (mean $\pm$ standard deviation).

State	KT(LH)	KT(TT)
Si^0	17.3$\pm$0.3	19.0$\pm$0.8
Si^{1+}	2.7$\pm$0.3	1.7$\pm$0.9
Si^{2+}	3.7$\pm$0.8	2.0$\pm$0.5
Si^{3+}	15.3$\pm$0.9	15.0$\pm$1.5
Si^{4+}	61.0$\pm$0.7	62.3$\pm$1.0

Table VI. Computed average mechanical properties based on KT(LH) and KT(TT)[26] potentials for ten independent a-Si (216 Si atoms) and a-SiO$_2$ (216 Si and 432 O atoms) structures. Strain was applied during mechanical property calculations using the same KT(LH) and KT(TT) potentials used during the initial CRN-MMC simulations. Relevant experimental data is also summarized for comparison.

	Y (GPa)	B (GPa)	
a-Si	124.3	83.4	KT(LH)
	158.4	85.7	KT(TT)
	125±1		Ref. 64
	136±9		Ref. 65
a-SiO$_2$	98.9	40.2	KT(LH)
	46.3	21.2	KT(TT)
	70	33.3	Ref. 66
	76.6±7.2		Ref. 67
	73		Ref. 68
	144		Ref. 69

FIGURE CAPTIONS

Figure 1. Representative cluster models used for calculating Si-Si and Si-O bond lengths. Cluster models for other oxidation states (see Table II) are obtained by adjusting the number of O atoms from these models. For calculating Si-O bond lengths, the two Si atoms neighboring the central O atom retain the same oxidation state.

Figure 2. Variations (ΔE) in total energies (from DFT, present work optimization (KT(LH)), and optimization of Ref. 26 (KT(TT))) per bond of (a) c-Si (with 8 atoms) and (b) c-SiO$_2$ (β-cristobalite with 8 SiO$_2$ units) as a function of the ratio (L/L_0) of the strained lattice constant (L) to the equilibrium lattice constant (L_0).

Figure 3. Variations (ΔE) in total energies (from DFT, present work optimization (KT(LH)), and optimization of Ref. 26 (KT(TT))) of the cluster model (inset) as a function of Si-O-Si bond angle (θ).

Figure 4. Relative total energies per Si atom ($\Delta \hat{E}_{total}$) (from DFT, present work optimization (KT(LH)), optimization of Ref. 26 (KT(TT)), and extended Stillinger-Weber potentials proposed without (WT1) and with (WT2) suboxide penalties in Refs. 27 and 28) for a-SiO$_x$ (x = 0, 0.5, 1.0, 1.5, and 2.0) (64 Si and 64x O atoms) structures. All structures were constructed from CRN-MMC simulations based on the KT(LH) potential without suboxide penalty energies. For each x, four independent structures are represented. For x = 0.5, 1.0, and 1.5, the distributions of Si oxidation states are summarized in Table III.
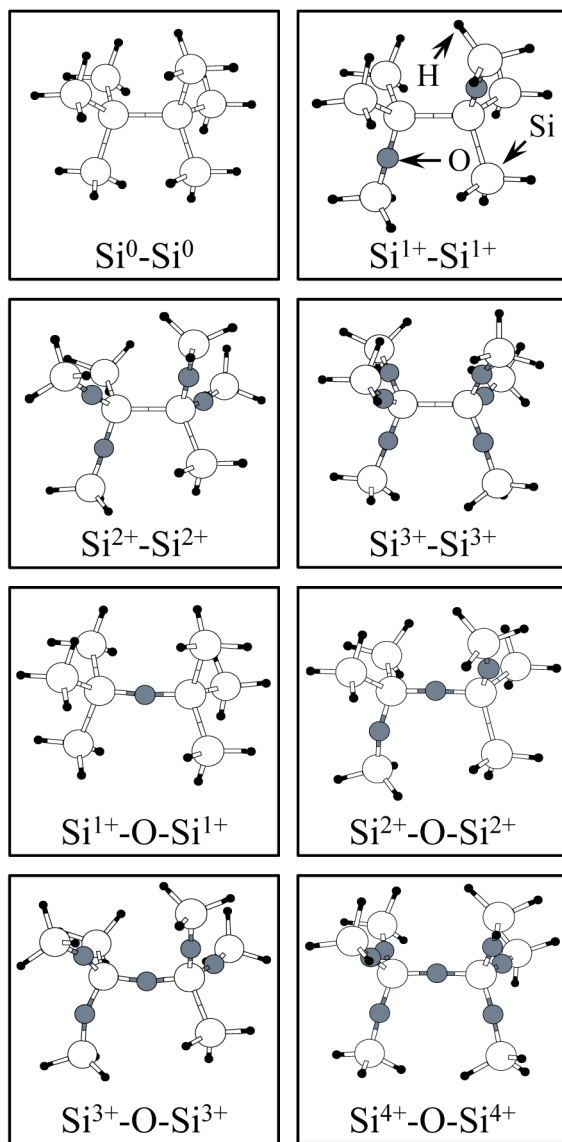
Figure 5. Average relative strain ($\Delta \hat{E}_{strain}$) and suboxide ($\Delta \hat{E}_{subox}$, insets) energies per Si based on KT(LH), KT(TT), and DFT calculations for a-SiO$_x$ (x = 0, 0.5, 1.0, 1.5, and 2.0) models constructed from CRN-MMC simulations based on the KT(LH) potential (a) excluding and (b) including suboxide penalty energies. For each x, four independent structures are represented. For x = 0.5, 1.0, and 1.5, the distributions of Si oxidation states for (a) and (b) are summarized in Tables III and IV, respectively.
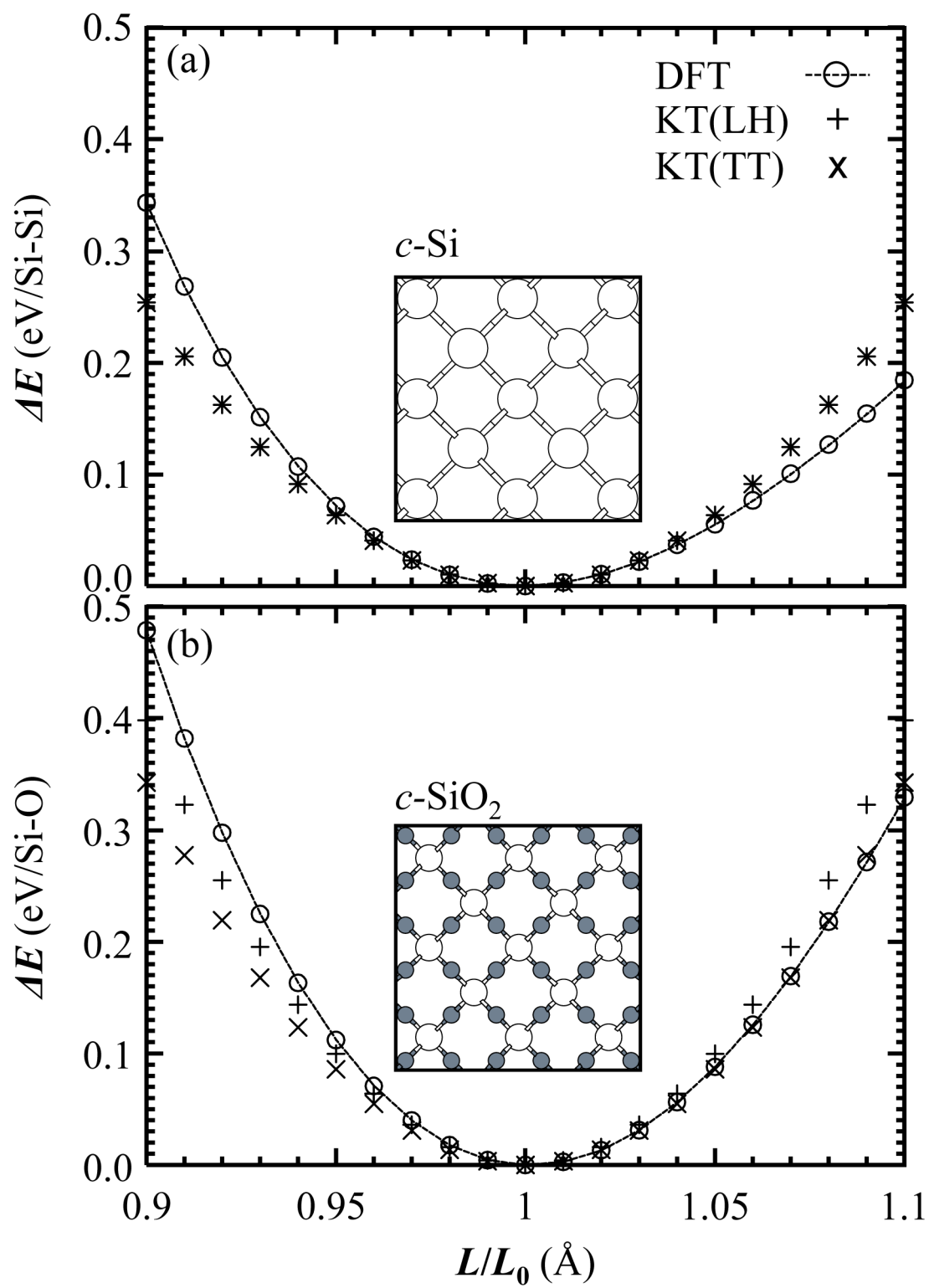
Figure 6. (Color online) Atomic configurations for (a) KT(LH) and (b) KT(TT) models for the a-Si cluster embedded in a-SiO$_2$ matrix (np-Si/a-SiO$_2$). Grey wireframe represents O atoms and Si^{4+} states that comprise the a-SiO$_2$ phase. Yellow, blue, red, and grey balls represent Si^0, Si^{1+}, Si^{2+}, and Si^{3+} states, respectively.
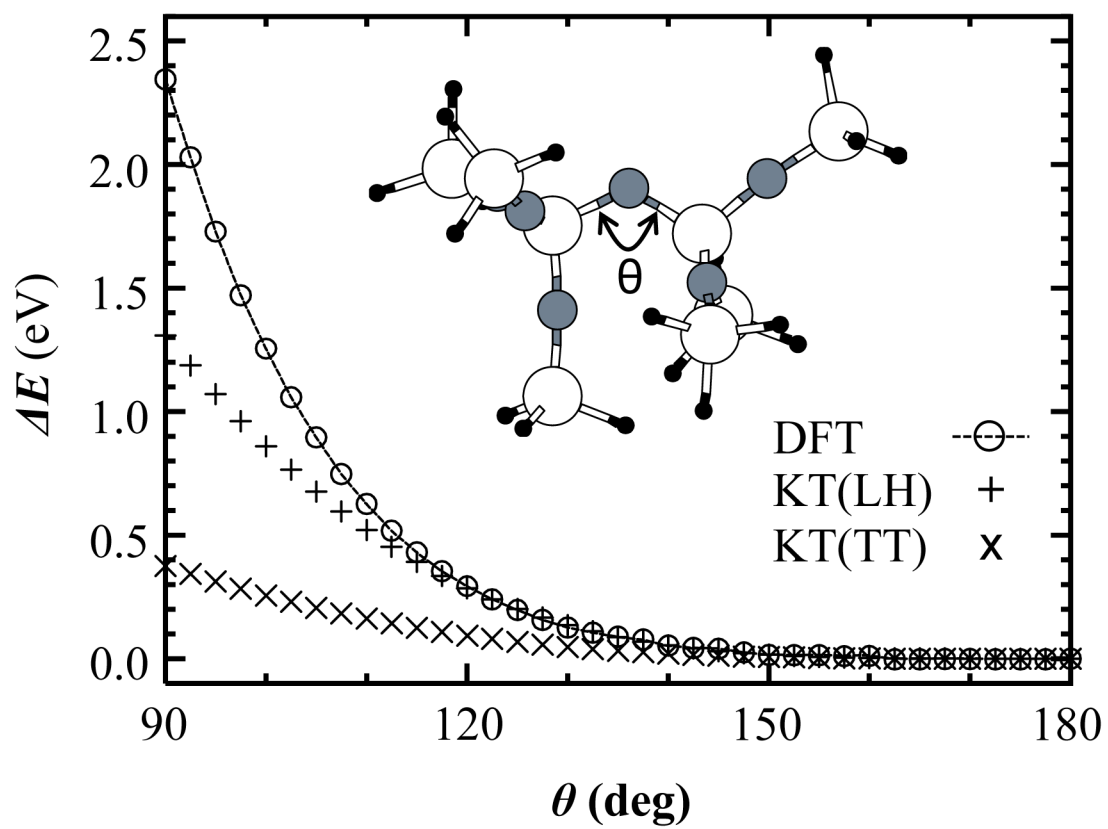
Figure 7. Profiles of (a) strain ($\Delta \hat{E}_{strain}$) and (b) suboxide ($\Delta \hat{E}_{subox}$) energies per Si along radial directions from cluster centers of KT(LH) and KT(TT) models for np-Si/a-SiO$_2$ (480 Si and 720 O atoms). The cluster center is defined as the center of mass of Si^0 atoms. The nominal interface radius, r_0, is defined in the text. Each data point represents the average value within a given concentric spherical shell (2 Å thick) sampled over four independent structures. The two solid, horizontal lines depict the calculated strain energies for bulk a-Si and a-SiO$_2$ with 216 Si and SiO$_2$ units, respectively. All energies are calculated with the KT(LH) potential.
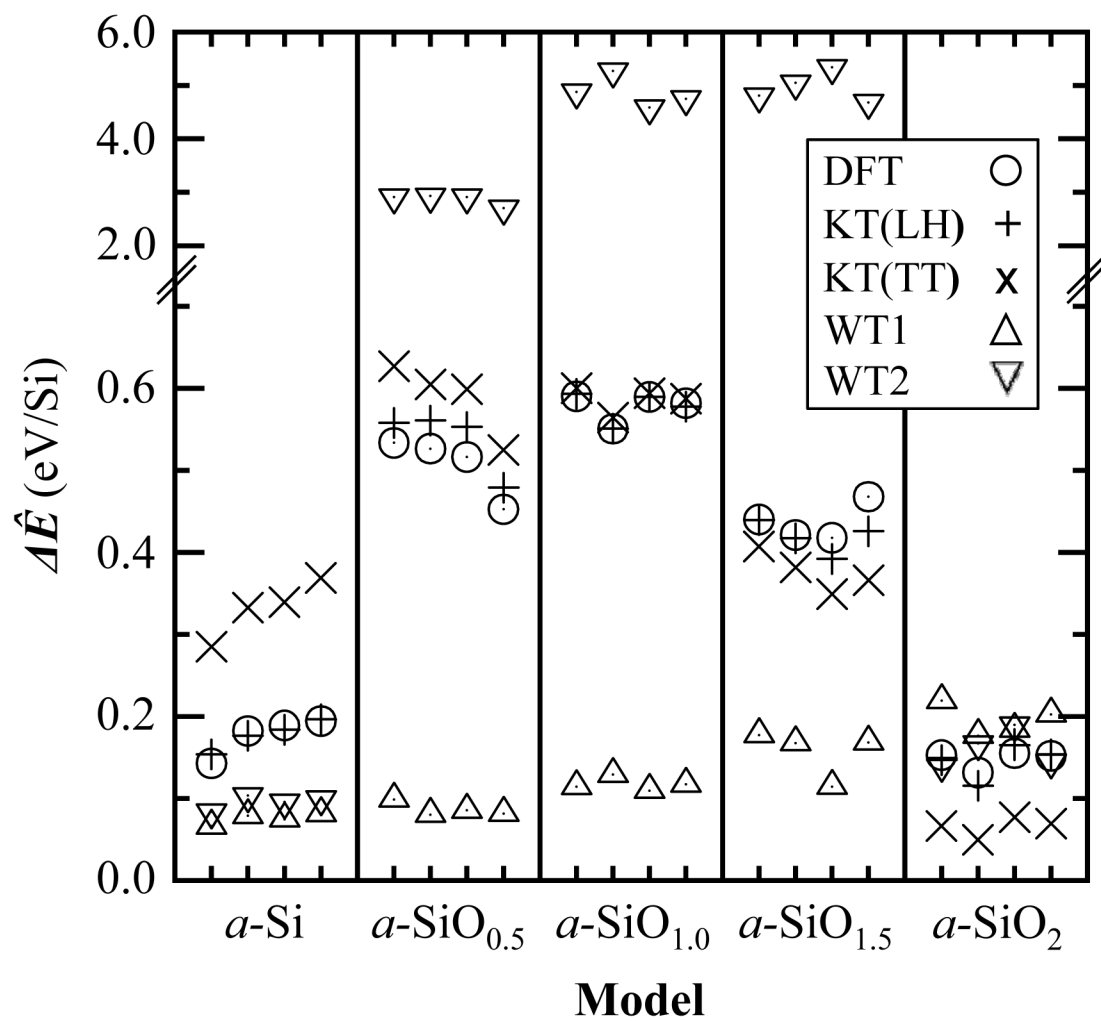
Figure 8. Profiles of (a) Si^{1+}, (b) Si^{2+}, and (c) Si^{3+} oxidation state distributions along radial directions from cluster centers of KT(LH) and KT(TT) models of np-Si/a-SiO$_2$ (480 Si and 720 O atoms). The cluster center is defined as the center of mass of Si^0 atoms. The nominal interface radius, r_0, is defined in the text. Each data point represents the average value within a given concentric spherical shell (2 Å thick) sampled over four independent structures.

Figure 9. Ring-size distributions for the (a) a-Si and (b) a-SiO$_2$ regions of KT(LH) and KT(TT) models of np-Si/a-SiO$_2$ (480 Si and 720 O atoms) together with the ring-size distributions for bulk (a) a-Si and (b) a-SiO$_2$ with 216 Si and SiO$_2$ units, respectively.

Si⁰-Si⁰   Si¹⁺-Si¹⁺

Si²⁺-Si²⁺   Si³⁺-Si³⁺

Si¹⁺-O-Si¹⁺   Si²⁺-O-Si²⁺

Si³⁺-O-Si³⁺   Si⁴⁺-O-Si⁴⁺

Figure 01   BV11090   18MAY2011

(a)

DFT   ⊖---
KT(LH)   +
KT(TT)   ✗

c-Si

(b)

c-SiO$_2$

ΔE (eV/Si-Si)

ΔE (eV/Si-O)

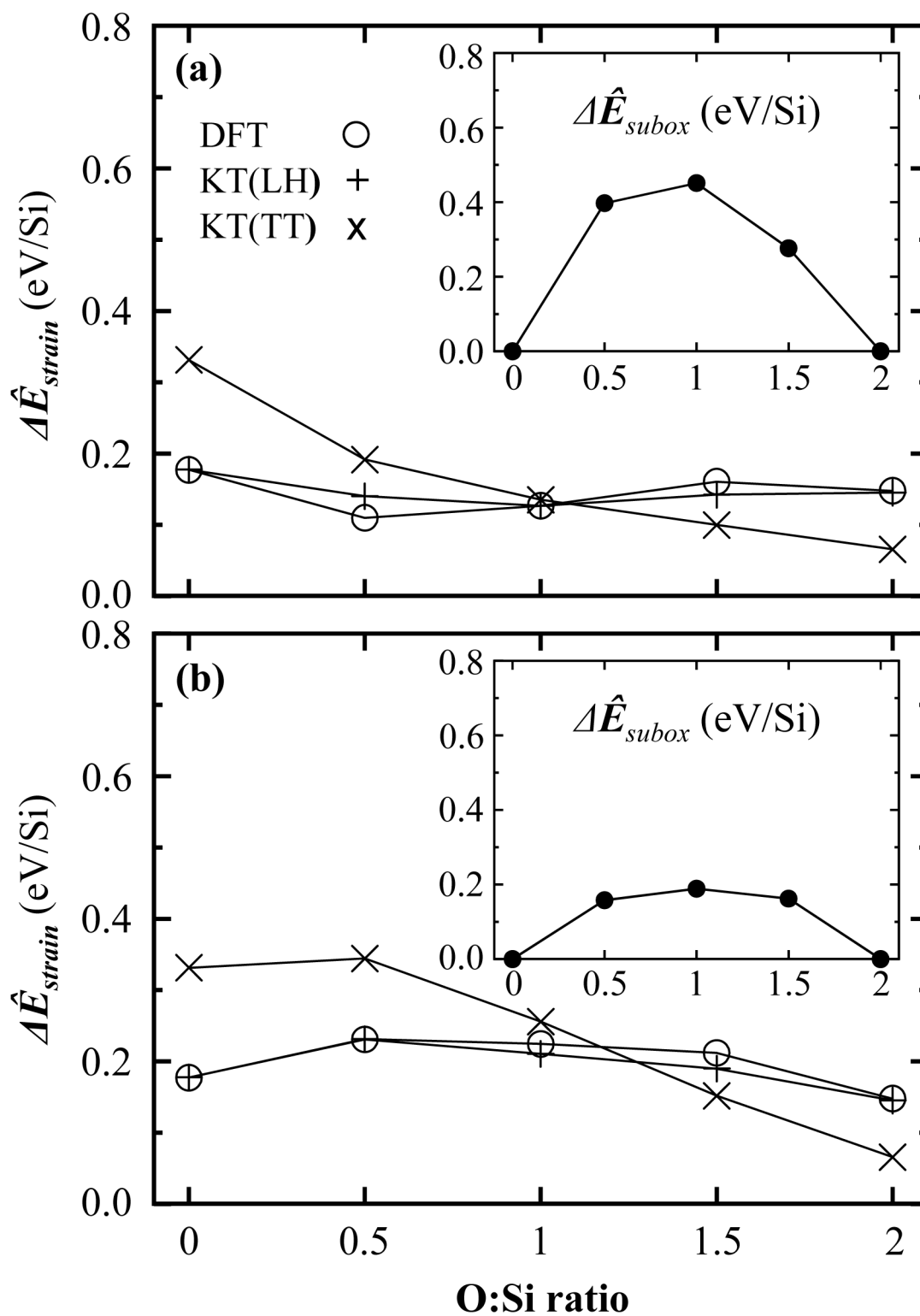L/L_0 (Å)

Figure 02   BV11090   18MAY2011

Figure 03   BV11090   18MAY2011

Figure 04   BV11090   18MAY2011

Figure 05   BV11090   18MAY2011
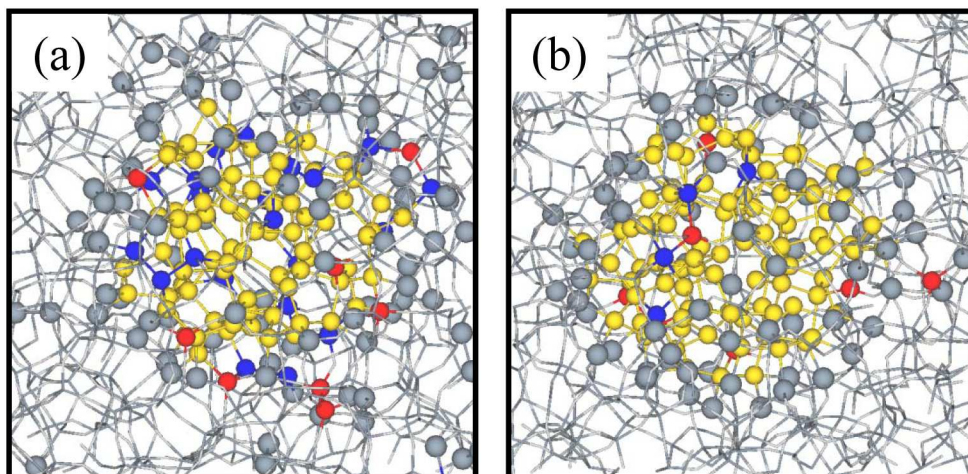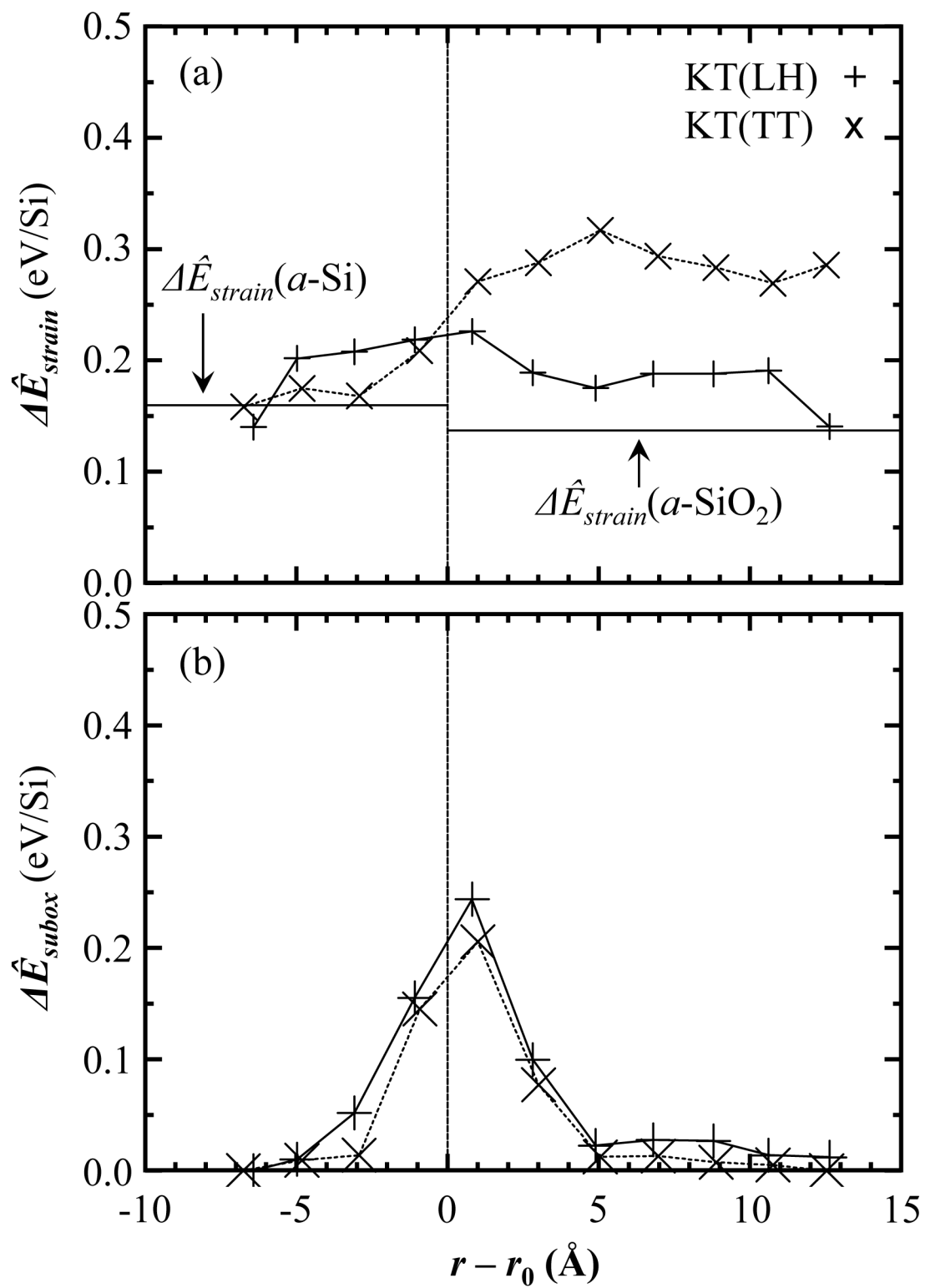
(a)

(b)

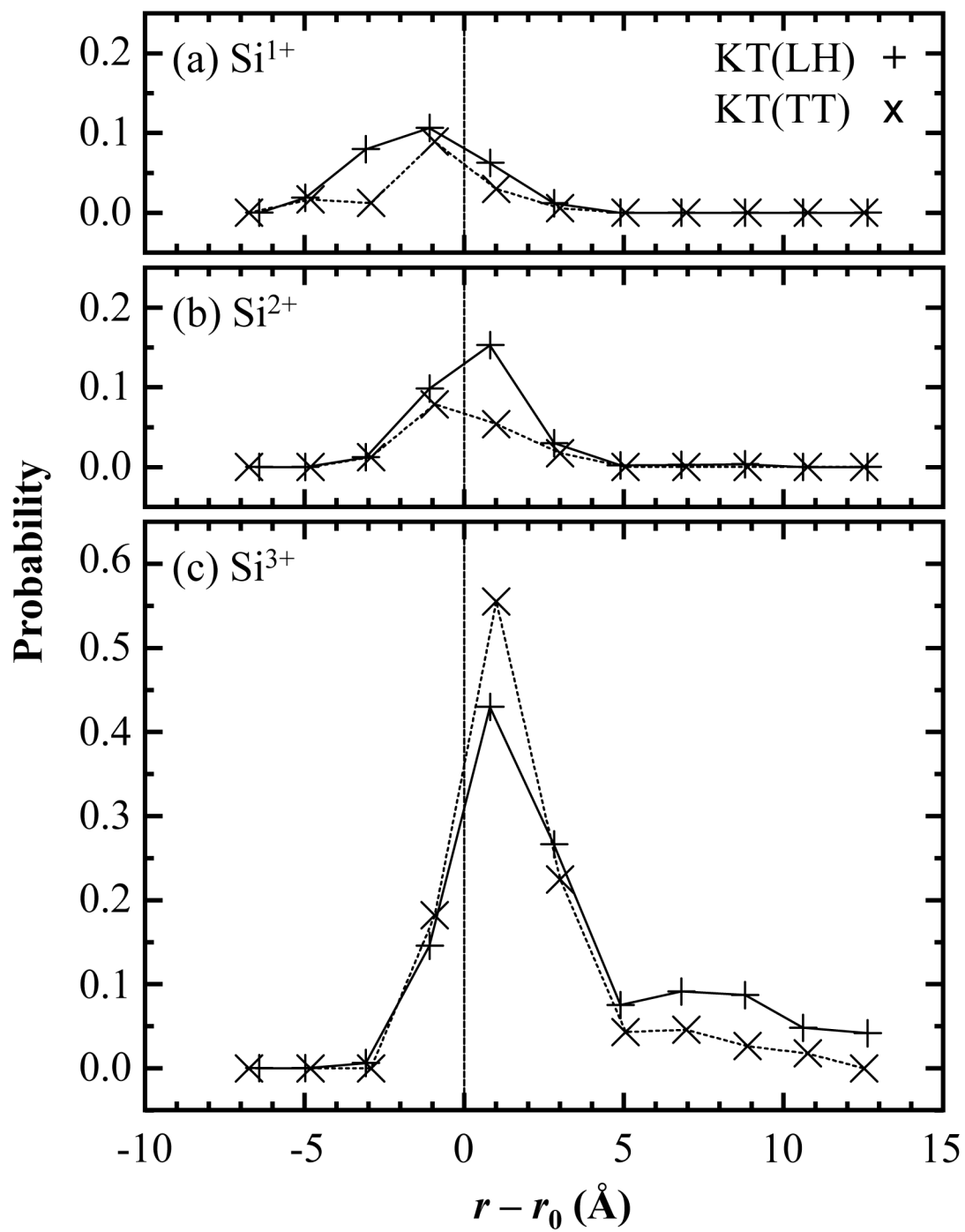Figure 06   BV11090   18MAY2011

Figure 07   BV11090   18MAY2011

Figure 08   BV11090   18MAY2011

Figure 09   BV11090   18MAY2011